Mid-infrared quantum cascade detectors for applications in spectroscopy and pyrometry

D. Hofstetter · F.R. Giorgetta · E. Baumann · Q. Yang · C. Manz · K. Köhler

Abstract In this paper, we give an overview of quantum cascade detector technology for the near- and mid-infrared wavelength range. Thanks to their photovoltaic operating principle, the most advanced quantum cascade detectors offer great opportunities in terms of high detection speed, reliable room temperature operation, and excellent Johnson noise limited detectivity. Besides some important features dealing with their fabrication and their general characteristics, we will also briefly present some possibilities for performance improvement. Elementary theoretical considerations adopted from photoconductive detectors confirm that optimization of such devices always involves various trade-offs.

1 Introduction

Although intersubband (ISB) photodetectors were first demonstrated already more than twenty years ago, they remain a topic of high scientific and practical interest. These early devices were photoconductive quantum well infrared photodetectors (QWIPs) [1]. It was soon discovered that

D. Hofstetter (✉)
University of Neuchatel, Avenue de Bellevaux 51,
2009 Neuchatel, Switzerland
e-mail: Daniel.Hofstetter@unine.ch
Fax: +41-32-7182901

F.R. Giorgetta · E. Baumann
Optoelectronics Division, National Institute of Standards and Technology, 325 Broadway, Boulder, CO 80305, USA

Q. Yang · C. Manz · K. Köhler
Fraunhofer Institute for Applied Solid State Physics,
Tullastrasse 72, 79108 Freiburg i. Brsg., Germany

QWIPs have many unique properties, especially regarding high frequency operation. As ISB detectors are unipolar devices, their fundamental speed limit is the ISB scattering time of electrons ($\tau_{scatter} \approx 1$ ps) rather than the parasitic capacitance of the p-n-junction or the finite transit time through the intrinsic region [2]. This typically results in cut-off frequencies on the order of 100 GHz [3]. As a further advantage, ISB detectors can be designed for a wide range of wavelengths using a single material system just by choosing adequate semiconductor layer thicknesses. This is in sharp contrast to interband devices, where the bandgap determines to a large extent the detectable photon energy.

An excellent overview on the different working principles of ISB infrared photodetectors is given in a book by Schneider and Liu [4]. In very basic terms, one can distinguish between photoconductive and photovoltaic detectors. In the class of photoconductive devices, the most common detector is the QWIP, where the change of device resistance under illumination is measured. There are several types of QWIPs; they differ mainly by the kind of ISB transition exploited. According to the position of the upper detector level, the optical transition can be either bound-to-quasi-bound [5] or bound-to-miniband [6]. In the widely used bound-to-quasi-bound QWIP, which was also the first ISB detector to be demonstrated in 1987, the detection energy depends on the conduction band discontinuity between the quantum well (QW) and the barrier material. The QW thickness and conduction band discontinuity (through the material composition) are chosen such that the second quantized electronic level is close to resonance with the barrier's conduction band edge; this measure ensures a good carrier extraction efficiency under application of an appropriate bias voltage. By using the bound-to-miniband design, the QWIP detection wavelength can be partly decoupled from the conduction band discontinuity. Nevertheless,

a resonance condition between the upper detector state and the miniband states must be fulfilled in order to obtain a good responsivity. Today, QWIP focal plane arrays sensitive at wavelengths between 8 μm and 10 μm have reached commercial maturity. As a particularly advanced example of such a QWIP-based camera, Gunapala et al. presented a high performance 1024 × 1024 pixel dual band focal plane array based on GaAs/AlGaAs with cutoff wavelengths of 5.1 μm and 8.4 μm [7]. The big advantages of such photoconductive ISB detectors are a high responsivity and a good detectivity, especially at low operating temperatures. However, their quite considerable dark current leads to a non-negligible dark current noise which dominates the noise budget at higher temperatures. This drawback is only partly compensated by the relatively high responsivity. In contrast, a photovoltaic ISB detector profits from the fact that there is no dark current and thus no dark current noise. Unfortunately, such a device has no photoconductive gain and therefore a lower responsivity, but the better noise behavior can at least partly make up for these shortcomings.

It is therefore somewhat astonishing that over the years, the development of photovoltaic ISB photodetectors has seen a slower overall progress. Already back in 1991, Schneider et al. [8, 9] observed pronounced photovoltaic effects in an asymmetric multi QW structure. The potential asymmetry was obtained via a sheet of delta-doping close to the active QW. As shown by Schneider as well, optimized photovoltaic QWIPs have superior noise properties, the capability to operate at higher photon fluxes, and an improved dynamical range in comparison to a photoconductive QWIP [10]. Especially with respect to the improved noise behavior, it is thus no surprise that the first QW-based infrared detector for THz radiation was a photovoltaic device rather than a photoconductive QWIP [11, 12]. A similar ISB detector for mid-infrared wavelengths was later presented by Gendron et al. [13]; in analogy to the functioning of a quantum cascade laser (QCL), this device was named quantum cascade detector (QCD). In such a QCD, the asymmetric potential used for unilateral carrier transport is formed by a series of QWs with increasing thicknesses. Interesting enough, a QCD-like semiconductor structure was invented already in 1987 under the name 'optical charge pump' [14]. Like the bound-to-miniband QWIP, this device offers more design freedom for a given material composition. A very schematic comparison between the band structures of a photoconductive QWIP and a photovoltaic QCD is shown in Fig. 1.

Compared to a QWIP, the absence of dark current noise is not the only advantage of a QCD. The missing dark current also prevents capacitance saturation in the read-out circuit and thus allows longer integration times. Finally, the thermal load of the detector is strongly reduced, which is of interest if the available cooling is limited, for example in space-born or hand-held terrestrial staring systems. As
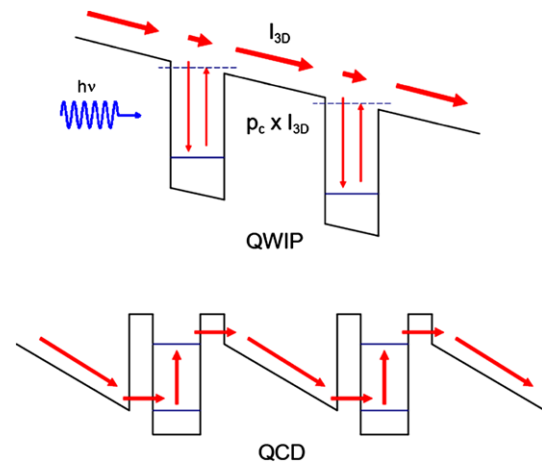

Fig. 1 Schematic conduction band diagram of a QWIP and a QCD. In the QWIP, electron transport is accomplished by an external voltage bias whereas in a QCD, an internal potential ramp ensures the carrier transport

a final point, the somewhat narrower linewidth of QCDs compared to QWIPs results in a reduced background photon noise. Although QCDs have already progressed a lot [15], they do not yet take full advantage of their potentially low Johnson noise; mainly because of an insufficiently high room temperature device resistance. Our most recent results, which will be presented in this paper, show nevertheless that QCDs with competitive performance can be achieved using improved designs.

We will discuss the design principles of QCDs as well as the choice of material system for the different detection wavelengths. Experimental results of QCDs at various wavelengths are reviewed. First, QCDs based on In-GaAs/InAlAs lattice matched to InP detecting between 4.7 μm and 10 μm are presented. As lattice matched In-GaAs QCDs can only detect wavelengths above ~4 μm due to the conduction band discontinuity of 520 meV, an alternative approach is presented for shorter wavelengths: strained InGaAs/InAlAs. Finally, a broadband QCD covering the wavelength region from 4.7 to 7.4 μm will be described. We will also discuss some of the trade-offs to be made when designing improved QCDs; they will lead to certain guidelines for detectors with particular applications.

2 QCD theory

The electro-optical behavior of QCDs can be described using exactly the same theory as in QWIPs. The basic optical process for mid-infrared detectors such as QWIPs or QCDs is the ISB transition [16]. In contrast to interband transitions, ISB transitions result in relatively narrow and peaked absorption features, whereas interband transitions are characterized by spectrally large absorption features with a cut-off

Table 1 General behavior of important QCD parameters as a function of the sheet carrier density, n_s, and the number of active QWs, N_{QW}

	η	g_p	$R_p \propto \eta \cdot g_p$	$D^*_{BLIP} \propto R_p/\sqrt{g_p^2\eta}$	R_0A	$D^*_J \propto R_p \cdot \sqrt{R_0A}$	T_{BLIP}
n_s small	n_s	const	n_s	$\sqrt{n_s}$	$1/n_s$	$\sqrt{n_s}$	const
n_s large	1	const	const	const	$1/n_s$	$1/\sqrt{n_s}$	↓
N_{QW} small	N_{QW}	$1/N_{QW}$	const	$\sqrt{N_{QW}}$	N_{QW}	$\sqrt{N_{QW}}$	const
N_{QW} large	1	$1/N_{QW}$	$1/N_{QW}$	const	N_{QW}	$1/\sqrt{N_{QW}}$	↓

wavelength. The main reason for this striking difference is the opposite curvature of the electron and hole dispersion curves in the interband case and the parallel curvature of the electronic subbands in the ISB case. The current responsivity of a QCD, R_p, is defined as detector output current I_S per unit of input signal power P_S and is given by

$$R_p = \frac{I_S}{P_S} = \frac{q}{h\upsilon}\eta g_p = \frac{\lambda q}{hc}\eta g_p; \quad g_p = \frac{p_e}{N_{QW}p_c} \quad (1)$$

where $\upsilon = c/\lambda$ is the signal frequency, λ the signal wavelength, c the vacuum speed of light, q the elementary charge, h Planck's constant, η the absorption efficiency, and g_p the photodetector gain. Furthermore, p_e is the escape probability of an excited electron in the active QW, p_c its capture probability into the active QW ground state, and N_{QW} the number of active QWs. Optimization of R_P is thus accomplished through improvement of both absorption efficiency and photodetector gain. For sufficiently low absorptions, the total absorption efficiency is proportional to the absorption efficiency of a single QW. However, since the detector gain is inversely proportional to the number of QWs, the current responsivity is in first approximation independent of the number of periods.

Another common figure of merit for photodetectors is the detectivity $D^* = R_p/i_n\sqrt{A\Delta f}$, which is the ratio between peak responsivity R_p and mean noise current i_n (or the inverse noise equivalent power) normalized by the detector area A and the measurement bandwidth Δf. Its units are cm Hz$^{0.5}$/W, also known as Jones. For any given infrared detector, the detectivity D^* reveals two distinct temperature regimes. At low temperatures, D^* is dominated by photon noise due to the 300 K blackbody radiation seen by the device. This is the background limited operating (BLIP) regime. Above a certain temperature, T_{BLIP}, other noise mechanisms become dominant. For a QWIP, D^* at $T > T_{BLIP}$ is determined by dark current noise, whereas the detectivity of a QCD is dominated by Johnson noise. Taking into account these different facts, we get for the detectivity of a QCD

$$D^*_J = R_p\sqrt{\frac{R_0A}{4k_BT}}$$

$$D^*_{BLIP} = \frac{R_p}{\sqrt{2q^2g_p \int g_p\eta(\nu')\frac{d\Phi_{BG}(\nu')}{d\nu'}d\nu'}} \quad (2)$$

where R_0 is the differential device resistance around 0 V, T the device temperature, and $d\Phi_{BG}(\nu')/d\nu'$ the spectral background photon flux density. For a QCD, D^* is maximized by ensuring a high device resistance (thus a low Johnson noise) without lowering the escape probability and thus the detector gain. The most important design parameters are the layer thicknesses (determining the band profile as discussed below), the doping density n_s of the active QW, and the number of periods N_{QW}.

Let us first have a look at the dependency on the doping density (sheet carrier density) n_s (see also Table 1). As long as the absorbance is small, $N_{QW}\alpha_{2D} \ll 1$, so that $\eta = 1 - \exp(-N_{QW}\alpha_{2D}) \approx N_{QW}\alpha_{2D}$, the absorption efficiency η and thus the responsivity R are proportional to α_{2D} and thus to the doping density n_s [15]. Looking at (2), it follows that D^*_{BLIP} is proportional to $\sqrt{n_s}$. As the device resistance decreases proportionally in $1/n_s$, D^*_J is proportional to $\sqrt{n_s}$ as well. In this case, T_{BLIP} remains constant. This does, however, not imply that n_s should be as high as possible. The absorption efficiency η cannot become larger than 1 and therefore saturates for too high doping concentrations. For high n_s, R and D^*_{BLIP} therefore saturate, whereas $D^*_J \propto 1/\sqrt{n_S}$ decreases with a further increase of n_s. This leads to a decrease in T_{BLIP} as well.

Similar considerations can be made regarding the dependency on the number of periods N_{QW}. Assuming again that $N_{QW}\alpha_{2D} \ll 1$ (small absorption) and thus $\eta \propto N_{QW}$, R is independent of the number of periods N_{QW} and D^*_{BLIP} increases with $\sqrt{N_{QW}}$. As the device resistance grows linearly with N_{QW}, the Johnson noise dependent detectivity D^*_J shows the same behavior as D^*_{BLIP}: $D^*_J \propto \sqrt{N_{QW}}$. This means again that T_{BLIP} does not change. For large N_{QW}, the aforementioned assumption of small absorption is not true anymore, η and D^*_{BLIP} saturate, R is proportional to $1/N_{QW}$, and D^*_J is proportional to $1/\sqrt{N_{QW}}$: T_{BLIP} decreases. As a conclusion, we notice that for any given doping density, an ideal number of periods must be found. This is also shown in Fig. 2 where a two-dimensional plot of D^*_J as a function of the number of periods and the doping density is shown. If—for instance—the doping density is increased (at constant number of periods), the responsivity increases as well. However, the resistance goes down, leading to a maximum in D^*_J. The same effect can be seen when increasing the number of periods (at constant doping density). Although the resistance

Fig. 2 Two-dimensional representation of the Johnson-noise limited detectivity of a QCD. The simulation is based on (1) and (2) and was done for a 7.5 μm device at 100 K
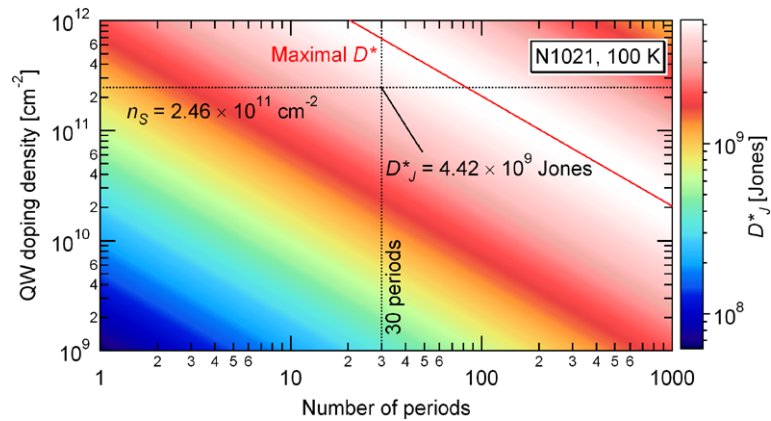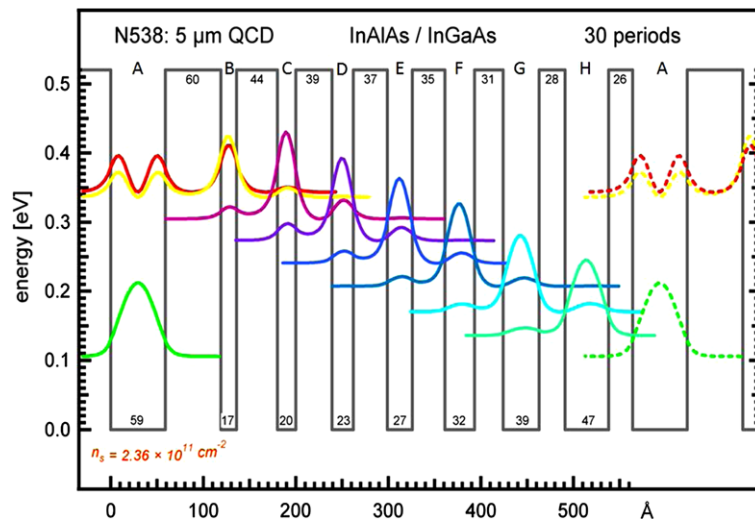
Fig. 3 Calculated conduction band profile of a QCD for 5.3 μm. QW A is the active QW, QWs B to H form the extractor cascade

goes up, the responsivity will start to decrease: in total, we will again get a maximum in the detectivity.

3 QCD design

The quantum-mechanical polarization selection rule [17] dictates that only the electric field component perpendicular to the QW layers interacts with ISB transitions. Therefore, vertical incidence of the incoming radiation has to be avoided. Possible device geometries taking into account the polarization selection rule include a 45° wedge multi-pass geometry, the Brewster geometry, or a surface grating. The particular choice of sample preparation is determined by factors such as the absorption strength of the sample or the specific application case of the detector.

The most crucial design aspect of ISB devices is the quantum-mechanical band structure. It can be calculated using numerical Schrödinger equation solvers. A typical band structure of a QCD is shown in Fig. 3. QW A is the active doped QW, while QWs B–H form the nominally undoped electron extraction cascade. The transport from the

active QW into the extraction region is guaranteed via a resonant tunneling process between the excited state in the active QW, A, and the ground state of QW B; this allows for a thick barrier between the active QW and the extractor. To achieve an efficient electron extraction through phonon assisted scattering, the energy difference between the individual extractor states should be close to the longitudinal optical phonon energy E_{LO} (GaAs: $E_{LO} = 36$ meV, $In_{0.53}Ga_{0.47}As$: $E_{LO} = 32$ meV).

4 QCD devices

There are various photodetector applications in the mid-infrared spectral range. They include pyrometry, spectroscopy, night vision, and sensing of hot spots. In the first part of this section, experimental results obtained from QCDs sensitive at wavelengths between 4.7 μm and 9.8 μm (126 meV–268 meV) are presented. The investigated samples consist of $In_{0.53}Ga_{0.47}As$ QWs and $In_{0.52}Al_{0.48}As$ barriers lattice matched to InP substrates. All layer structures were grown by molecular beam epitaxy (MBE) in order to

Fig. 4 Responsivity of the ISB main transition of a 9.8 μm device (*left*), a 7.5 μm device (*center*), and a 4.7 μm QCD (*right*) at 300 K along with the room temperature absorption spectra
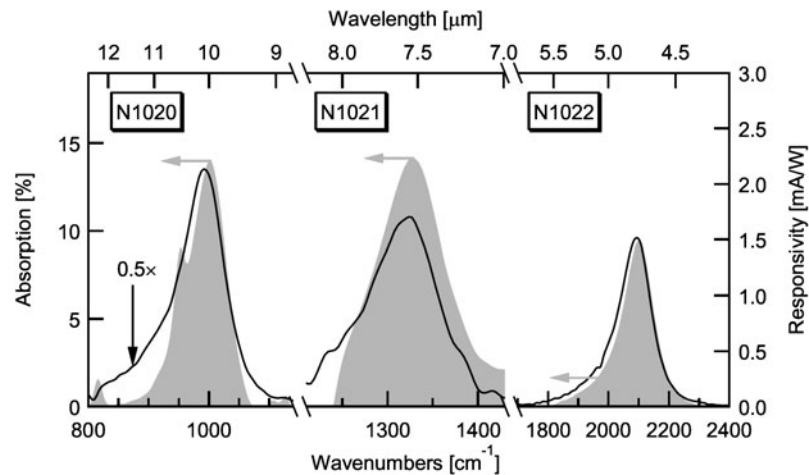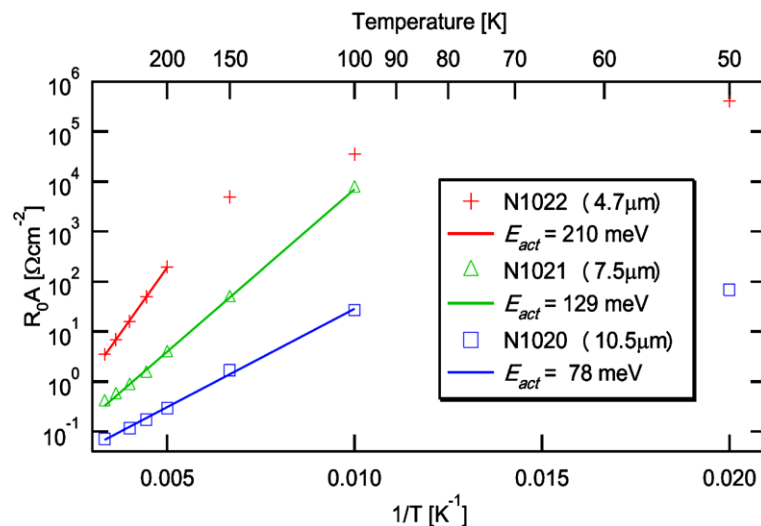
Fig. 5 Logarithmic representation of the R_0A-product of the three QCDs (4.7 μm: *cross symbols*, 7.5 μm: *upward triangles*, 10 μm: *squares*) shown in the previous figure as a function of inverse temperature. We observe activation energies of 210 meV for the 4.7 μm detector, 129 meV for the 7.5 μm device, and 78 meV for the 10.5 μm QCD

achieve a high interface quality between QWs and barriers. Growth started with a 6000 Å thick $In_{0.53}Ga_{0.47}As$ lower contact layer followed by 30 repetitions of the active region and a 2000 Å thick $In_{0.53}Ga_{0.47}As$ upper contact layer. Details on the layer thicknesses can be found in reference [18]. From a design point of view, the samples shown here are based on the QCDs presented in reference [19]. They have, however, thicker barriers to increase device resistance. After growth, the samples were polished into 45° multi-pass waveguides for absorption tests; for photocurrent measurements, mesas were processed using standard photolithography and wet etching. Contacting was obtained through evaporated metal contacts.

Figure 4 shows the measured responsivity spectra of the three samples for temperatures at 300 K. These responsivity spectra need to be compared with the grey-shaded absorption spectra. Excellent agreement is observed. For the two shorter wavelength samples, the peak detection energies of 268 meV/2144 cm^{-1} and 168 meV/1344 cm^{-1} correspond well to the simulated ones of 266 meV/2128 cm^{-1}

and 165 meV/1320 cm^{-1}, respectively. For the longer wavelength sample, the observed value of 127 meV/1016 cm^{-1} is slightly too large with respect to the designed 118 meV/944 cm^{-1}. Figure 5 shows the R_0A-products for all three samples as a function of inverse temperature. Activation energies of 210 meV, 168 meV, and 78 meV were observed for the 4.7 μm, 7.6 μm, and 9.8 μm samples, respectively. Via (2), we calculated a background-limit temperature and detectivity of $T_{BLIP} = 45$ K and 2×10^{11} Jones, respectively, for the 4.7 μm QCD. Because of their lower device resistances, the two other QCDs show detectivities remains below D^*_{BLIP} for all investigated temperatures. They reach values of 5×10^9 Jones at 100 K for the 7.5 μm QCD and 9×10^8 Jones at 100 K for the 9.8 μm QCD.

The conduction band discontinuity of the lattice-matched $In_xGa_{1-x}As/In_yAl_{1-y}As$ heterostructures can be increased from the lattice-matched value of 520 meV at $x = 0.53$, $y = 0.52$ by raising the In content above 53% in the InGaAs QW and reducing it below 52% in the InAlAs barrier. However, the modified In contents introduce strain be-
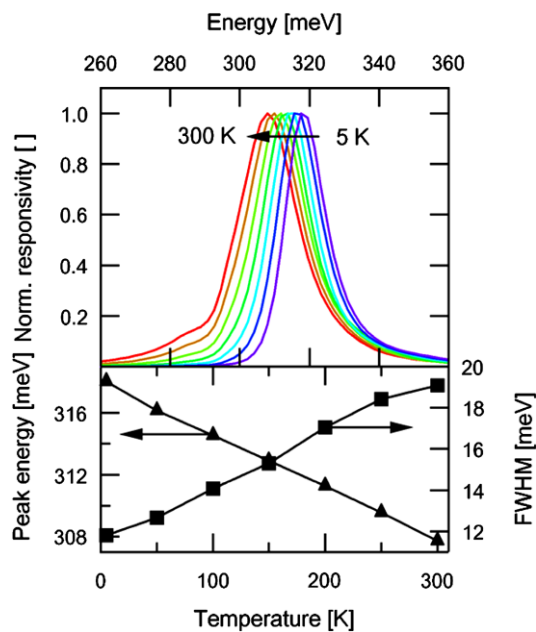
Fig. 6 *Top*: temperature evolution of the responsivity spectra of the strained InGaAs/InAlAs QCD between 5 and 300 K. *Bottom*: energy of peak responsivity and spectral linewidth as a function of temperature. The relative linewidth increases from 4.4% at 5 K to 6.6% at 300 K and the temperature tuning coefficient is -0.275 cm^{-1}/K

tween the barrier and QW layers and the InP substrate. Since these strains are of opposite sign, namely tensile in the barrier and compressive in the QW, a nearly strain compensated pseudomorphic active region can be obtained by choosing appropriate layer thicknesses and material compositions. Using strained $In_{0.61}Ga_{0.39}As/In_{0.42}Al_{0.55}As$ with a band discontinuity of 610 meV [20], a 10 period QCD with a peak detection energy of 319 meV (3.88 μm) could be fabricated [21]. Its active region consisted of 60% barrier material; hence a small residual strain of 0.1% towards the InP substrate remained. Due to the relatively small total thickness of the detector, this small lattice mismatch did not lead to a relaxation of the crystal. The measured responsivity shown in Fig. 6 (top) has a maximum value of 10.7 mA/W at 318 meV (3.9 μm) and 150 K. The measured transition energy corresponds well to the simulated ISBT energy of 319 meV, demonstrating that both growth and simulation of 0.5% strained InGaAs/InAlAs heterostructures have a high maturity just as the lattice-matched InGaAs/InAlAs. Inserting the measured room temperature peak absorption per double pass of 6% and the corresponding peak responsivity of 5.8 mA/W at 300 K into (1) results in a 30% escape probability p_e of photoexcited electrons from the main QW into the extractor. The Johnson noise limited detectivity D_J^* of this short wavelength QCD was calculated with the measured R_0A and peak responsivities; it equals 4.9×10^7 Jones at 300 K and reaches the background limited detectivity $D_{BLIP}^* = 1.2 \times 10^{11}$ Jones (for 300 K background temper-

ature and a hemispherical FOV) at $T_{BLIP} = 108$ K. The evolution of the linewidth and the responsivity peak position is shown at the bottom of Fig. 6.

A potential application for fast mid-infrared photodetectors is heterodyne spectroscopy, which allows distinguishing spectrally close absorption lines. This spectroscopic method requires mid-infrared detectors capable of multi-GHz operation. In order to obtain a preliminary estimation on the frequency response of a 5.46 μm QCD, such a device was tested using an optical heterodyne beat setup [22]. For this experiment, the detector was held at room temperature. The optical input signal was generated by two collinearly overlaid CW operated distributed feedback QCLs with identical emission wavelengths around 5.4 μm. By modifying the drive current of one of the QCLs, its emission frequency was slightly shifted resulting in a beat signal with a repetition rate equal to the difference frequency between the QCLs. The detector response showed a second order lowpass characteristic which could be described with an RLC circuit taking into account the input impedance of the amplifier R, the parasitic capacitance of the QCD, C, and the bond wire inductance, L. The corner frequency was 4 GHz and the cutoff frequency 23 GHz. Our simple theoretical model confirmed that the frequency response was limited by the sample mount. Due to the ultra-fast phonon-electron scattering, a cutoff frequency of roughly 65 GHz is expected for these detectors, similar as with the QWIPs presented in reference [2].

5 Outlook

Figure 7 shows an overview of the different QCDs fabricated so far in our labs. One can see that there exist three material families, which fall into the three interesting wavelength ranges. There are GaAs/AlGaAs devices for the far-infrared (84 μm, not shown in the figure), InGaAs/InAlAs detectors for the mid-infrared (3.9–17.5 μm), and InGaAs/AlAsSb QCDs for the near-infrared wavelength range (2.1–2.5 μm). It is quite obvious that the detectivities of the shorter midinfrared devices are closest to the theoretical maximum. Therefore, any future effort will without any doubt concentrate on an improvement of the detectivity of QCDs in the technologically most important 5–10 μm range. Samples N973 and N975 show also a very high detectivity, but they had to be cooled to 5 K to achieve these good values. The reason for their high resistance and thus nearly ideal detectivity was the use of regular superlattice extraction regions with a relatively poor conductivity in growth direction. For each specific application of a QCD, a different set of parameters needs to be optimized. For a detector in pyrometry, the responsivity close to room temperature should be as large as possible, while spectrally narrow detection

Fig. 7 Detectivity as a function of detection wavelength for all near- and mid-infrared QCDs presented in this article. It is obvious that the devices between 4.7 μm and 10 μm offer a considerable potential for improvement
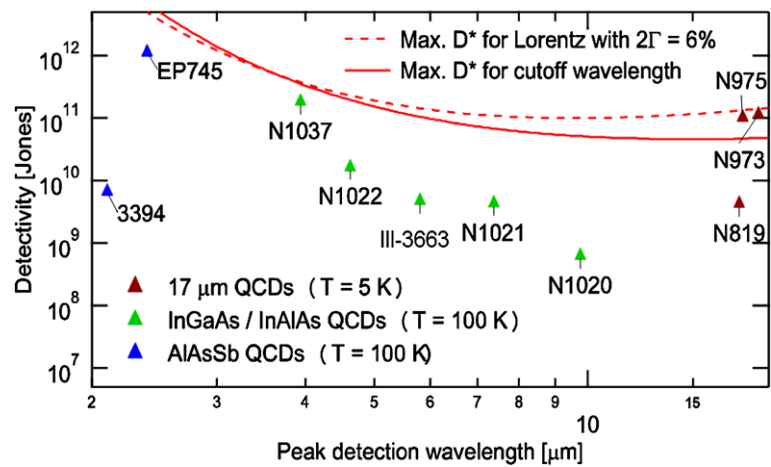
is not necessarily an advantage. In highly sensitive spectroscopy applications, a narrow detection window together with a good detectivity would be highly desirable. For applications such as heterodyne spectroscopy, high frequency operation would be required. In a night vision system, finally, one would like to have a good detectivity, but not necessarily at room temperature. Such a system could very well function at cryogenic temperatures and at low frequencies. Several of the requirements of such a hypothetical wish list are contradictory; therefore, one has to make trade-offs. For instance, someone could be tempted to increase the room temperature resistance by making very thick barrier layers. This would result in a better Johnson noise behavior, but since thick barriers will decrease the tunneling probabilities, the detector would certainly end up slower than before. Or in an effort to increase the responsivity against spectrally broad blackbody radiation, one might try to make a broadband detector. But this will increase the background noise floor and therefore decrease the *BLIP* detectivity of the QCD. Here, we review briefly some possibilities for improved detectors:

Recently, a spectrally broad mid-infrared QCD based on lattice-matched InGaAs/InAlAs with a relative linewidth of 27% was designed and fabricated [23]. It made use of 26 carefully designed active region stages spanning a wavelength range between 4.7 and 7.4 μm. The device worked with a responsivity in excess of 10 mA/W at 150 K and 1.5 mA/W at 300 K. The detectivity was somewhat lower than in a standard narrowband QCD, but still acceptably high ($D^*_{\mathrm{BLIP}} = 2 \times 10^{10}$ Jones at $T_{\mathrm{BLIP}} = 40$ K).

As already stated above, pyrometers should possess a good detector response at temperatures close to 300 K. For this purpose, one has first to grow thick barriers to reduce the electron-phonon scattering rates between adjacent periods and to secondly push all extractor states towards higher energy using thinner QW layers. Due to a reduced ground state coupling and less thermal activation of electrons, these measures will result in a considerably higher device resistance, especially at room temperature. Since the resistance

does not only improve the Johnson noise limited detectivity, but also prevent leakage currents in the device, this will definitely increase QCD performance in terms of response. On the other hand, thicker barriers will slightly reduce the detection speed. In Fig. 8, we show simulated resistance-area products for the 4 μm QCD shown previously, and for an improved version of it. It is obvious that there occurs a factor of 100 in the $R_0 A$-product which results in a factor of 10 improvement in the Johnson noise limited detectivity.

For high-speed operation, it is clear that phonon resonance and efficient scattering processes in the extraction region are an absolute necessity. For this reason, barrier layer thicknesses should not be too large. As the 23 GHz cutoff frequency of a QCD in this article have shown, a more sophisticated sample mounting adapted to high frequency operation will have a positive effect on the detector speed. Together, these measures should enable detector operating frequencies closer to the theoretical maximum.

6 Conclusions

QCDs are a promising technology which has proven to work well at wavelengths from the near infrared to the THz region as presented in Fig. 7. The design process of QCDs is reliable and robust. Especially in the mid-infrared range around 4 to 17 μm, well established semiconductor material systems and processing methods are available. Accordingly, we demonstrated QCDs in the near-IR fabricated from InGaAs/AlAsSb, in the mid-IR using InGaAs/InAlAs, and in the THz-region using GaAs/AlGaAs materials. A chirped QCD design is a first step towards semiconductor-based ISB detectors for spectrally broad applications. Together with the high speed and design flexibility, this makes QCDs very interesting candidates for applications in this wavelength range. Considerable margin for improvement, especially in terms of room temperature detectivity and responsivity, has been identified.

Fig. 8 Simulated
resistance-area-products for the
4 μm QCD shown in Fig. 6 in its
current configuration (thin
barriers, low extractor states)
and in the improved version
(thick barriers, pushed up
extractor states)
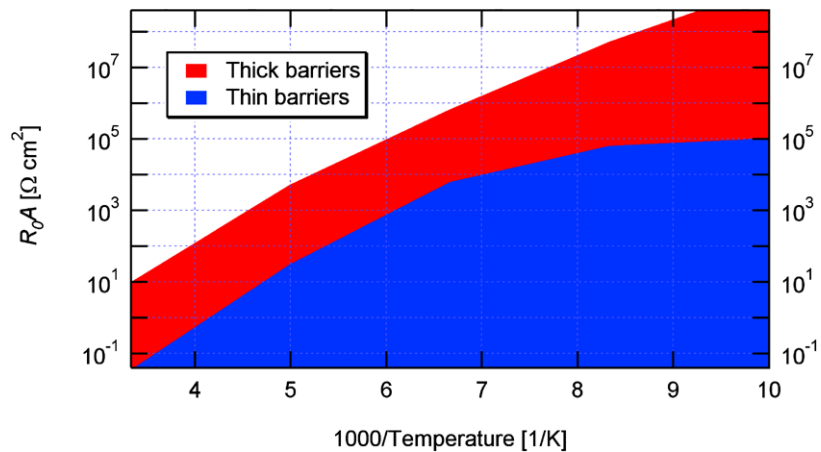
References

 1. B.F. Levine, K.K. Choi, C.G. Bethea, J. Walker, R.J. Malik, Appl.
    Phys. Lett. **50**, 1092 (1987)
 2. P. Bhattacharya, *Semiconductor Optoelectronic Devices*, 2nd edn.
    (Prentice-Hall, Englewood Cliffs, 1997), pp. 364–368
 3. H.C. Liu, J.M. Li, E.R. Brown, K.A. McIntosh, K.B. Nichols, M.J.
    Manfra, Appl. Phys. Lett. **67**, 1594 (1995)
 4. H. Schneider, H.C. Liu, *Quantum Well Infrared Photodetectors*
    (Springer, Berlin, 2006)
 5. H.C. Liu, J. Appl. Phys. **73**, 3062 (1993)
 6. K.M.S.V. Bandara, J.W. Choe, M.H. Francombe, A.G.U. Perera,
    Y.F. Lin, Appl. Phys. Lett. **60**, 3022 (1992)
 7. S.D. Gunapala, S.V. Bandara, J.K. Liu, C.J. Hill, S.B. Rafol, J.M.
    Mumolo, J.T. Trinh, M.Z. Tidrow, P.D. LeVan, Infrared Phys.
    Technol. **47**, 67 (2005)
 8. H. Schneider, P. Koidl, F. Fuchs, B. Dischler, K. Schwarz, J.D.
    Ralston, Semicond. Sci. Technol. **6**, C120 (1991)
 9. H. Schneider, K. Kheng, M. Ramsteiner, J.D. Ralston, F. Fuchs, P.
    Koidl, Appl. Phys. Lett. **60**, 1471 (1992)
10. H. Schneider, J. Appl. Phys. **74**, 4789 (1993)
11. M. Graf, G. Scalari, D. Hofstetter, J. Faist, H. Beere, E. Linfield,
    D. Ritchie, G. Davies, Appl. Phys. Lett. **84**, 475 (2004)
12. H.C. Liu, H. Luo, C. Ying Song, Z. Wasilewski, A. SpringThorpe,
    J. Cao, IEEE J. Sel. Top. Quantum Electron. **14**, 374 (2008)
13. L. Gendron, M. Carras, A. Huynh, V. Ortiz, C. Koeniguer, V.
    Berger, Appl. Phys. Lett. **5**, 2824 (2004)
14. M.A. Reed, US patents #4'878'104 (1987) and #5'165'065
    (1992)
15. L. Gendron, C. Koeniguer, V. Berger, X. Marcadet, Appl. Phys.
    Lett. **86**, 121116 (2005)
16. M. Helm, *The Basic Physics of Intersubband Transitions*. Semi-
    conductors and Semimetals, vol. 62 (Academic Press, London,
    2000)
17. H.C. Liu, M. Buchanan, Z. Wasilewski, Appl. Phys. Lett. **72**, 1682
    (1998)
18. F.R. Giorgetta, E. Baumann, M. Graf, Q. Yang, C. Manz, K. Köh-
    ler, H.E. Beere, D.A. Ritchie, A.G. Davies E Linfield, Y. Fedo-
    ryshyn, H. Jäckel, M. Fischer, J. Faist, D. Hofstetter, IEEE J.
    Quantum Electron. **45**, 1039 (2009)
19. M. Graf, N. Hoyler, M. Giovannini, J. Faist, D. Hofstetter, Appl.
    Phys. Lett. **88**, 241118 (2006)
20. D. Hofstetter, M. Beck, T. Aellen, J. Faist, Appl. Phys. Lett. **78**,
    396 (2001)
21. F.R. Giorgetta, E. Baumann, R. Theron, M.L. Pellaton, D. Hof-
    stetter, M. Fischer, J. Faist, Appl. Phys. Lett. **92**, 121101 (2008)
22. D. Hofstetter, M. Graf, T. Aellen, J. Faist, L. Hvozdara, S. Blaser,
    Appl. Phys. Lett. **89**, 061119 (2006)
23. D. Hofstetter, F.R. Giorgetta, E. Baumann, Q. Yang, C. Manz, K.
    Köhler, Appl. Phys. Lett. **93**, 221106 (2008)